Testing of Sr-Doped ZnO/CNT Photocatalysts for Hydrogen Evolution from Water Splitting under Atmospheric Dielectric Barrier Plasma Exposure

Muhammad Irfan, Saba Afzal, Muzammil Hussain, Muhammad Yasin Naz,* Shazia Shukrullah, Saifur Rahman, Salim Nasar Faraj Mursal, and Abdulnour Ali Jazem Ghanim

ACCESS | 📊 Metrics & More | 📖 Article Recommendations

ABSTRACT: Nonthermal plasma is a well-recognized environmentally advanta- geous method for producing green fuels. This work used different photocatalysts, including PZO, S_xZO, and S_xZC_x for hydrogen production using an atmospheric argon coaxial dielectric barrier discharge (DBD)-based light source. The photocatalysts were produced using a sol−gel route. The DBD discharge column was filled with water, methanol, and the catalyst to run the reaction under argon plasma. The DBD reactor was operated with a 10 kV AC source to sustain plasma for water splitting. The light absorption study of the tested catalysts revealed a decrease in the band gap with an increase in the concentration of Sr and carbon nanotubes (CNTs) in the Sr/ZnO/CNTs series. The photocatalyst $S_{25}ZC_2$ demonstrated the lowest photoluminescence (PL) intensity, implying the most quenched recombination of charge carriers. The highest H_2 evolution rate of 2760 μmol h^{-1} g^{-1} was possible with the $S_{25}ZC_2$ catalyst, and the lowest evolution rate of 56 μmol h^{-1} g^{-1} was observed with the PZO catalyst. The photocatalytic activity of $S_{25}ZC_2$ was initially high, which decreased slightly over time due to the deactivation of the photocatalyst. The photocatalytic activity decreased from 2760 to 1670 μmol h^{-1} g^{-1} at the end of the process.
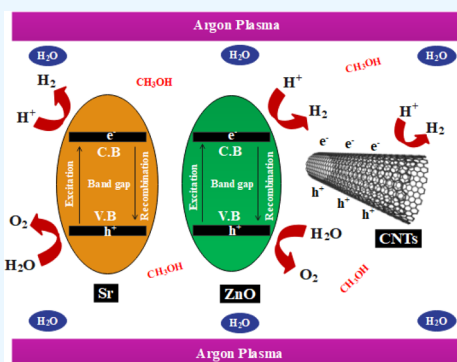
1. INTRODUCTION

Excessive use of fossil fuels has resulted in an unavoidable energy crisis and global pollution. Therefore, a low-cost and eco-friendly strategy is important for current issues to fulfill the demand for energy utilization. H_2 can be utilized as a byproduct to generate power with the water reaction and has a much higher energy content of 122 kJ g^{-1} than hydrocarbons and is considered a promising energy source for the next generation.[1] Many techniques have been used for hydrogen generation to meet the energy demand. H_2 gas evolution, observed via modern technologies by using steam reforming and fossils, is 48 and 95%, respectively. By using the partial oxidation process, the 30 and 18% hydrogen production corresponds to the hydrocarbons and coal.[2] Being a continuous and pollutant-free process, water splitting for the photocatalytic evolution of hydrogen is viewed as an ideal fuel for a sustainable future. The production of hydrogen through photocatalytic overall water splitting is an exciting method. The photocatalytic efficiency, however, falls short of expect- ations. Analysis of the obstacles to total photocatalytic water splitting is thus important.[3]

ZnO nanoparticles have attracted significant interest due to their environmentally friendly nature, cost-effectiveness, and high quantum yield among semiconductor photocatalysts.[4]

The high oxidation ability of ZnO with surface reactivity and strong chemical ability due to O_2 nonstoichiometry ensures the creation of abundant defects sites. The generation of these defects makes the ZnO photocatalyst a potential candidate for photocatalytic activity applications.[5] Having a binding energy of ∼60 meV and band gap energy of ∼3.3 eV, ZnO is characterized for light absorption in the UV region. For industrial applications, the photocatalytic ability of these nanoparticles is not sufficient due to their small surface area.[6] To overthrow these constraints, ZnO is prepared in different ways, as reported by Esmaeilzadeh et al.[7] The photocatalytic performance of ZnO can assuredly be enhanced under visible light irradiation by doping with strontium (Sr). The optical properties of ZnO can be altered through doping, which significantly increases photocatalytic activity.[8] The photocatalytic performance of ZnO can also be improved by
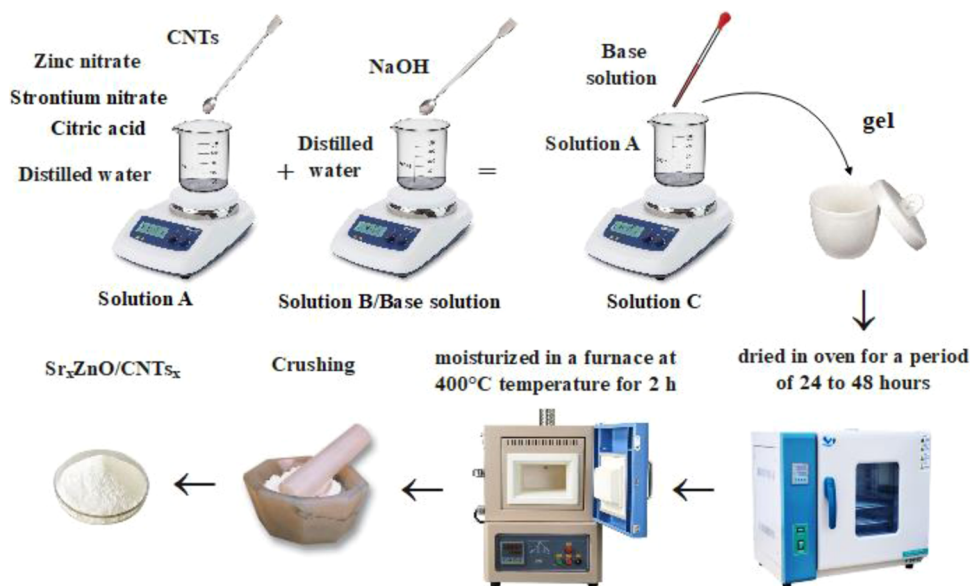
Figure 1. Illustration of steps involved in the production of $Sr_xZnO/CNTs_x$ photocatalysts.

modifying it with carbon nanotubes (CNTs). The electrons can easily move from the conduction band of zinc oxide to CNTs due to their low work function. CNTs accept electrons to enhance the separation of photoinduced electron−hole pairs, leading to a high H_2 evolution rate.[9] The excellent conductivity of CNTs, which improves H_2 production activity, accelerates the movement of charges to the plane of the catalyst. Hence, CNTs work as a transporter and an e^- sink in the photocatalyst. However, enough progress in this field is needed to reduce the hurdles in producing CNT-based composites for optimum hydrogen production, as revealed by Zhang et al.[10] The other photocatalysts, such as TiO_2/CNTs, have shown high hydrogen evolution efficiency due to low charge migration impedance and maximum surface area under visible light exposure.[11] Although ZnO/CNT composites have resulted in high hydrogen production, they still face severe challenges for commercial-scale applications. These challenges include inadequate visible light harvesting, low stability and strong photocorrosion, tiresome synthesis process, and scarcity of a detailed photocatalyst mechanism. Different metal-doped ZnO/CNT composites have been reported by various researchers.[12] Light absorption is increased by the lattice defects produced by alkaline earth metals due to the ionic radius and charge compensation mismatching between the host and alkaline metal. The photocatalyst formed of ZnO, CNTs, and a metal results in a multifaceted e^- transfer system, as reported by Hümmer et al.[13]

In the literature review, it was found that photocatalysts for water-splitting applications have different rates of hydrogen production. Ahmad et al.[14] reported 2683 $\mu mol\ h^{-1}\ g^{-1}$ hydrogen production with a Tb−ZnO/CNT photocatalyst after 5 h of reaction under visible light. Lin et al.[15] produced a $Pt/TiO_{2-x}N_x$ photocatalyst by using a two-microemulsion method for H_2 evolution. After 6 h of reaction, they reported 475 μmol of H_2 evolution at room temperature under visible light. Argon was used as a carrier gas to improve the reaction efficiency in dielectric barrier discharge (DBD) plasma.[16] In the presence of argon plasma, H_2 production rates were also compared for $BaLa_4Ti_4O_{15}$ and NiO for CO_2−H_2O photocatalysts.[17,18] Kawawaki et al.[17] evaluated the hydrogen

evolution rate of a $BaLa_4Ti_4O_{15}$ photocatalyst with 16% apparent quantum yield after 10 h of reaction time. Yao et al.[18] investigated a NiO photocatalyst for CO_2−H_2O conversion into CO, H_2, and CH_4 by using a DBD reactor. They reported 21.0, 354.3, and 0.061 $\mu mol\ h^{-1}\ g_{act}^{-1}$ yield rates of CO, H_2, and CH_4, respectively, at room temperature. El-Shafie et al.[19] used an argon−water vapor mixture for H_2 generation with a DBD plasma exposure. The maximum H_2 concentration rate at 20 °C and 7.3 kV was 1500 ppm. In this paper, the maximum H_2 gas production occurred under argon DBD plasma at room temperature within 4 h of reaction time. DBD plasmas are being used more frequently as UV sources. They are utilized as UV radiation sources for everything from producing ozone for industry to excimer radiations. Low-pressure high-output UV lamps have a mercury content of 26−150 mg, compared to 5−50 mg for low-pressure UV lamps. A significant quantity of poisonous mercury waste with detrimental effects on both human health and the environment is produced at the end of the lamp's life. In this study, a DBD-based mercury-free light source reactor was chosen over other reactors because it can be easily made into different sizes and shapes, thanks to its insulating design and free electrode. This makes it easy to fit it into a specific application. The other reason to choose a DBD reactor is that it ensures a controllable process under atmospheric conditions, even in dark environments. The plasma-born reactive species and radiation in the visible to ultraviolet range derive the hydrogen evolution reaction without sunlight.[20−22] In this study, the photocatalytic hydrogen evolution tests were performed using ZnO, Sr-doped ZnO (Sr_xZnO), and Sr-doped ZnO/CNT ($Sr_xZnO/CNTs_x$) photocatalysts. The maximum H_2 evolution was observed with the $S_{25}ZC_2$ photocatalyst. The proposed photocatalytic mechanism or better H_2 evolution is also discussed in this work.

2. EXPERIMENTAL PART

2.1. Materials. Zinc nitrate ($Zn(NO_3)_2$), citric acid, strontium nitrate ($Sr(NO_3)_2$), carbon nanotubes (CNTs), and NaOH were used in the synthesis of photocatalysts.

Methanol (CH_3OH) was used as a sacrificial agent in the water-splitting reaction.

2.2. Preparation of Photocatalysts. The steps involved in preparation of pure ZnO, Sr-doped ZnO (Sr_xZnO), and Sr-doped ZnO/CNT ($Sr_xZnO/CNTs_x$) photocatalysts are illustrated schematically in Figure 1. A facile sol−gel method was followed to prepare these photocatalysts. The ZnO sample was prepared by adding 10 g of citric acid and 4.44 g of zinc nitrate in 100 mL of distilled water under continuous heating and stirring for 40 min. The as-obtained solution was collected in a crucible and dried at 120 °C for 30 h and then calcinated at 400 °C for 3 h. After calcination, the as-prepared sample was ground to obtain a fine powder of the ZnO photocatalyst. A similar route was followed to produce Sr-doped ZnO with different contents of strontium nitrate (0.5, 1.09, and 1.35 g). For the $Sr_xZnO/CNTs_x$ sample, 0.14 g of purified CNTs was added into the mixture before drying in the oven and forming solution A. A homogeneous solution (base solution or solution B) was obtained by dissolving 15 g of NaOH into 70 mL of distilled water. Solution B was added to solution A with a dropper to obtain pH 9 under continuous stirring. The obtained solution was heated to remove moisture and calcinated at 400 °C for 2 h. The end product was crushed to obtain a fine powder of the $Sr_xZnO/CNTs_x$ photocatalyst. Using a similar procedure, for a comparative study, a set of photocatalysts were prepared with different concentrations of zinc nitrate (3.09 and 3.64 g) and strontium nitrate (1.09 and 1.35 g), as shown in Table 1.

Table 1. Formulation of Samples with a Doping Percentage and Code

sr no.	sample	doping level	sample code
1	pure zinc oxide (ZnO)	Sr = (x = 0 wt %) and CNTs = (x = 0 wt %)	PZO
2	Sr-doped ZnO (Sr_xZnO) or S_xZO	Sr = (x = 10 wt %) and CNTs = (x = 0 wt %)	$S_{10}ZO$
3	Sr-doped ZnO (Sr_xZnO) or S_xZO	Sr = (x = 20 wt %) and CNTs = (x = 0 wt %)	$S_{20}ZO$
4	Sr-doped ZnO (Sr_xZnO) or S_xZO	Sr = (x = 25 wt %) and CNTs = (x = 0 wt %)	$S_{25}ZO$
5	Sr-doped ZnO/CNTs ($Sr_xZnO/CNTs_x$) or S_xZC_x	Sr = (x = 10 wt %) and CNTs = (x = 2 wt %)	$S_{10}ZC_2$
6	Sr-doped ZnO/CNTs ($Sr_xZnO/CNTs_x$) or S_xZC_x	Sr = (x = 20 wt %) and CNTs = (x = 2 wt %)	$S_{20}ZC_2$
7	Sr-doped ZnO/CNTs ($Sr_xZnO/CNTs_x$) or S_xZC_x	Sr = (x = 25 wt %) and CNTs = (x = 2 wt %)	$S_{25}ZC_2$

2.3. DBD-Assisted Hydrogen Evolution. In this work, a coaxial DBD-based mercury-free light source setup was designed that generated both visible and UV radiations, as shown in Figure 2a. UV radiation was typically found in the range of 200−400 nm. The geometry of the reactor uses two coaxial quartz tubes (Figure 2b). An inner electrode is separated by a dielectric barrier enclosed in the envelope bounded by an outer electrode, known as the mesh electrode. The mesh allows the radiation to escape from the lamp envelope. When AC power is supplied, the ozonizer discharge is generated between the electrodes. When inert gases are used to make a discharge, the DBD reactor also makes diatomic molecules. These radiations interact with solids, gases, and liquids in different ways.[23] In this study, argon was used as plasma gas. A 10 kV AC power supply with a 50 Hz frequency was used to power the DBD reactor. About 5 g of PZO, S_xZO,
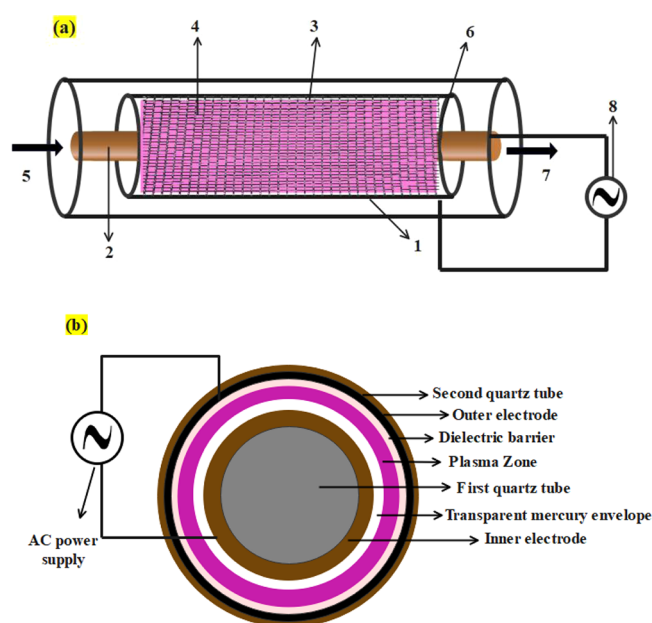

Figure 2. (a) Coaxial DBD-based mercury-free light source used for water splitting. (1) First quartz tube, (2) inner electrode, (3) plasma zone, (4) mesh electrode or outer electrode, (5) inlet, (6) transparent envelope wrapped around the inner electrode, (7) outlet, and (8) AC power supply. (b) Coaxial shape of the DBD-based mercury-free light source.

and S_xZC_x photocatalysts were loaded one by one into the DBD reactor and activated using plasma-born radiation. The activated catalyst is then used in water splitting to produce hydrogen. Due to the decomposition of water under plasma exposure, oxygen gas is also emitted from the reactor along with hydrogen. A gas analyzer was used to examine both gases. When exposed to plasma, water rapidly separates into hydrogen and oxygen in the presence of the photocatalyst, providing twice as much hydrogen as oxygen.

3. RESULTS AND DISCUSSION

3.1. Fourier Transform Infrared (FTIR) Study of the Photocatalyst. FTIR spectra of S_xZC_x photocatalysts were recorded within the range of 500−3500 cm^{-1}, as shown in Figure 3. The FTIR analysis showed characteristic peaks at 1429 cm^{-1} for $S_{10}ZC_2$, which are assigned to the O−H bending of a carboxylic acid group. The photocatalytic activity of catalysts depends on the amount of −OH groups, which are the source of highly reactive •OH radicals.[24] The peak at 1429 cm^{-1} refers to the O−H bending of water molecules, as reported by Beena et al.[25] The second peak of the same catalyst was found in the fingerprint region at 865 cm^{-1}, which displayed a strong appearance (out of plane) with C−H bending. The IR spectrum peaks at 1314 and 773 cm^{-1} exhibited the C−O stretching and C−H bending vibrations of $S_{10}ZC_2$ and $S_{20}ZC_2$ photocatalysts. The FTIR peak at 773 cm^{-1} in both spectra confirms the bending vibration of Zn−O.[26] The compound class, group region, and peak appearance of the S_xZC_x photocatalyst are shown in Table 2.

3.2. X-ray Diffraction (XRD) Study. XRD spectra of $S_xZC_{x'}$, as reported in Figure 4, demonstrated six diffraction peaks around $2\theta°$ values of 32.2, 34.7, 38.2, 44.3, 53.6, and 62.9°. These peaks can be indexed to the (100), (002), (101), (102), (110), and (103) diffraction planes of hexagonal
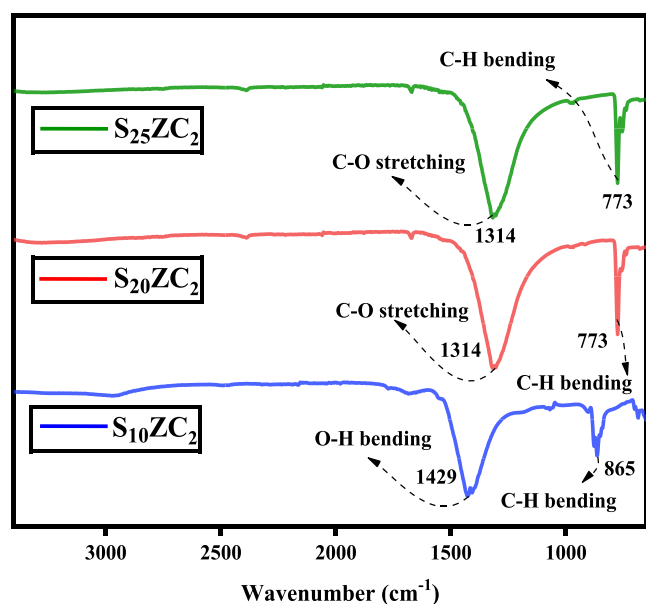
Figure 3. FTIR spectra of $S_{10}ZC_2$, $S_{20}ZC_2$, and $S_{25}ZC_2$ photocatalysts.

Table 2. FTIR Peaks, Appearance, Groups, and Compound Class of S_xZC_x Samples

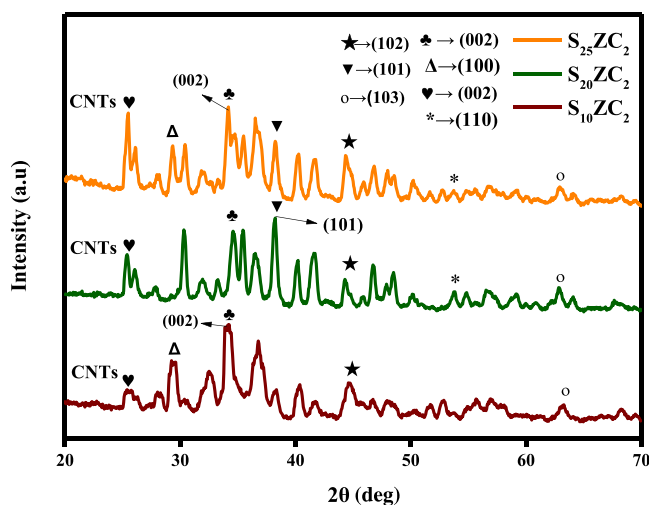| FTIR peaks	groups	compounds class	peaks appearance	group region
1314	C−O stretching	aromatic ester	strong	GFR
1429	O−H bending	carboxylic acid	medium	GFR
773	C−H bending	1,2,3-trisubstituted	strong	FPR
865	C−H bending	1,3-disubstituted	strong	FPR

Figure 4. XRD spectra of $S_{10}ZC_2$, $S_{20}ZC_2$, and $S_{25}ZC_2$ photocatalysts.

wurtzite ZnO (JCPDS 36-1451), respectively.[27] Moreover, the S_xZC_x photocatalyst exhibited a diffraction peak of CNTs at 25.25°, which was perceived as (002) (JCPDF card. 20-0781) and corroborated the successful doping of CNTs into ZnO.[28] In modified S_xZC_x, diffraction peaks shifted slightly toward larger 2θ due to a smaller ionic radius of Zn^{2+} (0.074 nm) than Sr^{2+} (0.118 nm). This difference in radii distorts the host lattice of ZnO.[29] Some other peaks of photocatalysts that appeared at 37.60, 40.8, and 46.8° showed a doping content of

Sr^{2+} into the ZnO lattice as a substituent. The grain size of photocatalysts was determined by Scherrer's formula and exhibited an inverse relation with Sr concentration. Kaskun et al.[29] reported that the suppressed growth of crystals due to the addition of CNTs is the reason for a decreased crystallite size. The d-spacing values of crystals in Table 3 were calculated using Bragg's law.

Table 3. Data Extracted from the Analysis of XRD Spectra

photocatalyst	$2\theta°$	indices (hkl)	grain size (nm)
$S_{10}ZC_2$	34.7	(002)	0.52
$S_{20}ZC_2$	38.2	(101)	2.08
$S_{25}ZC_2$	34.7	(002)	0.52

3.3. Optical Study. The UV−vis spectra of the photocatalyst S_xZC_x are shown in Figure 5. The photoabsorption of $S_{10}ZC_2$, $S_{20}ZC_2$, and $S_{25}ZC_2$ samples in Figure 5a exhibited a blue shift at a wavelength of 366.68, 361.57, and 354.68 nm, respectively. Due to the combined effect of CNTs and Sr^{2+}, the structure of ZnO was changed and the flow of charges to the surface of composites was increased.[30] The absorbance intensity values of S_xZC_x with a band gap energy are also displayed in Table 4. The optical band gap energy values of $S_{10}ZC_2$, $S_{20}ZC_2$, and $S_{25}ZC_2$ decreased with increasing the doping content of Sr. This decrease in the band gap is attributed to the synergistic effect between graphene and Sr-doped ZnO, as shown in Figure 5b−d. The relation of Kubelka−Munk ($\alpha h\nu = A(h\nu - E_g)^{n/2}$) was utilized for the calculation of band gap energies of $S_{10}ZC_2$, $S_{20}ZC_2$, and $S_{25}ZC_2$ photocatalysts as 2.27, 2.22, and 1.94 eV, respectively.[31]

The photoluminescence (PL) technique is used to study the transfer capability and recombination efficiency of charge carriers in the catalyst.[32] A high photoemission intensity usually indicates strong recombination of charge carriers. Figure 7 represents the PL spectra of S_xZC_x photocatalysts at room temperature. The PL of S_xZC_x was observed by using the excitation wavelength at 300 nm. Each spectrum of S_xZC_x displayed three different emission bands, such as the normal UV−visible emission of ZnO at 470 nm possessed recombination-free excitons. The orange band exhibited the emission between 420 and 450 nm that occurred due to surface defects in the lattice of ZnO. The green emission is due to the recombination of electrons that occupied single oxygen vacancies at 470 nm. The maximum PL intensity was observed for the least-doped photocatalysts.[33] The $S_{10}ZC_2$ photocatalyst demonstrated the maximum intensity and the lowest recombination of photoinduced charge carriers. In contrast, the PL intensity was the lowest for the $S_{25}ZC_2$ photocatalyst, denoting the highest inhibition ability of charge carriers due to the synergistic effect of Sr doping and CNTs as an electron sink.

3.4. Scanning Electron Microscopy (SEM) Morphological Analysis. SEM micrographs and the particle size distribution of S_xZC_x photocatalysts are shown in Figure 6. The material properties of CNTs were anticipated to be increased by the introduction of ZnO. The images displayed the bamboo-type structure of nanoholes in CNTs with effective doping of Sr in ZnO at room temperature.[34] Some CNTs were also observed in images were encapsulated by long clusters with a hexagonal wurtzite crystal structure of ZnO, which will be beneficial for electron transport to increase charge separation.[35] As the crystal is composed of grains and
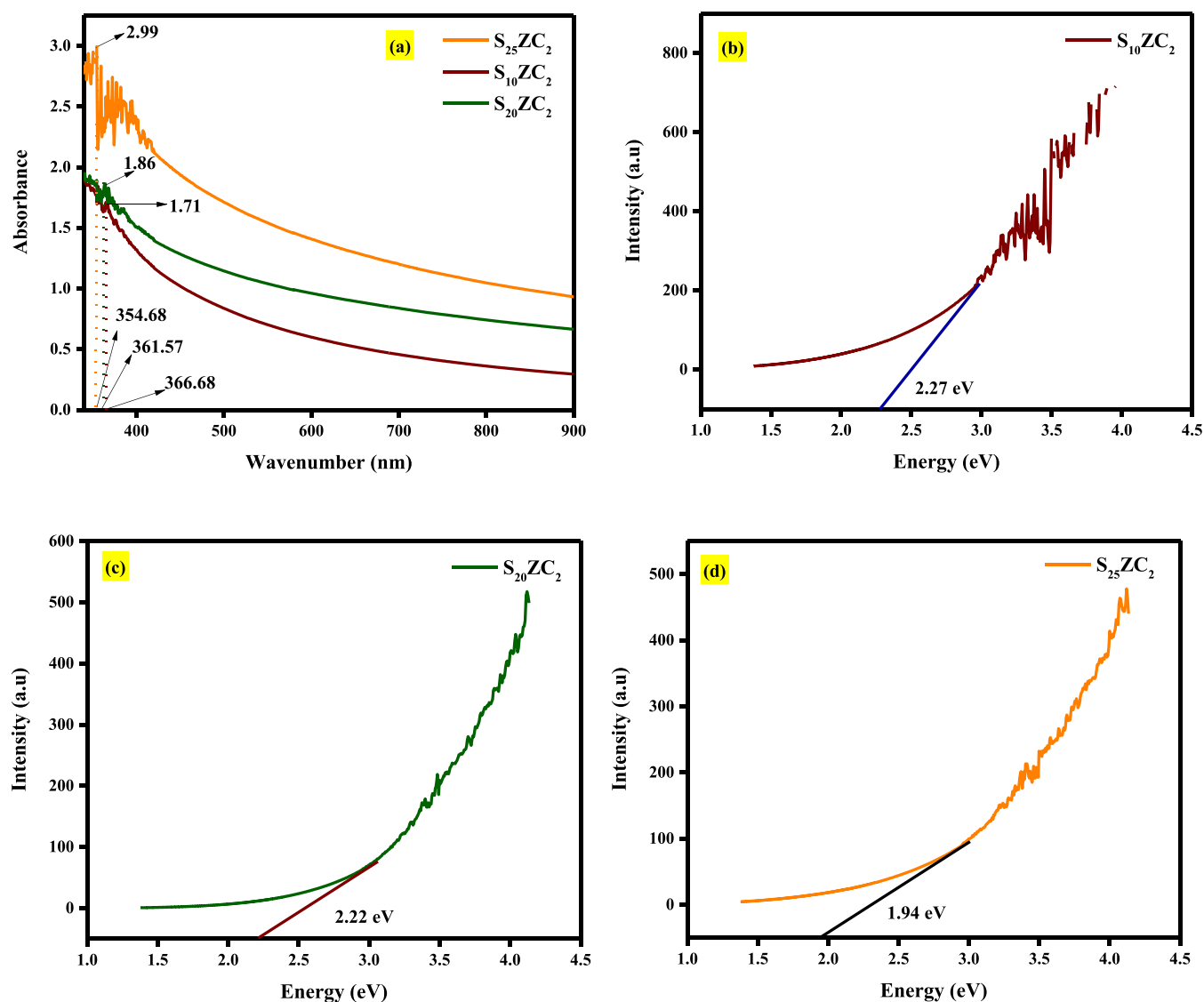
Figure 5. (a) UV−vis spectra of $S_{10}ZC_2$, $S_{20}ZC_2$, and $S_{25}ZC_2$ and (b−d) band gap estimation of $S_{10}ZC_2$, $S_{20}ZC_2$, and $S_{25}ZC_2$ samples, respectively.

Table 4. Absorbance and Band Gap Energies of $S_{10}ZC_2$, $S_{20}ZC_2$, and $S_{25}ZC_2$ Photocatalysts

photocatalyst	wavenumber (nm)	absorbance	band gap energy (eV)
$S_{10}ZC_2$	366.68	1.71	2.27
$S_{20}ZC_2$	361.57	1.86	2.22
$S_{25}ZC_2$	354.68	2.99	1.94

shows a smooth surface, by enhancing the Sr amount in ZnO, there is hardly a change in the particle size of crystals. The size of the as-prepared $S_{10}ZC_2$, $S_{20}ZC_2$, and $S_{25}ZC_2$ samples was measured to be about 63, 55, and 45 nm, respectively.[36]

3.5. Hydrogen Evolution. *3.5.1. Effect of Doping Concentration.* The photocatalytic response of as-prepared photocatalysts for H_2 evolution was checked under argon plasma through a DBD-based mercury-free light source reactor. The outcomes are reported in Figure 7. These findings suggested that the minimum evolution rate of 56 μmol h^{-1} g^{-1} for the PZO photocatalyst is due to its wide band gap and fast photoinduced charge carriers recombination rate. The reaction rate increased for Sr-doped ZnO (S_xZO) photocatalysts compared to that of PZO by adding the Sr content in pure

zinc oxide.[37] The hydrogen evolution efficiency of $S_{25}ZO$, $S_{10}ZO$, and $S_{20}ZO$ photocatalysts was measured to be about 1150, 695, and 901 μmol h^{-1} g^{-1} under identical research conditions. The hydrogen evolution rate increased at room temperature with the introduction of CNTs in the S_xZO photocatalyst. The maximum hydrogen evolution of 2760 μmol h^{-1} g^{-1} was possible with the $S_{25}ZC_2$ photocatalyst, which reveals the central role of CNTs in boosting the separation of photoinduced charge carriers. It is clear that H_2 production is related to the doping content of Sr in the presence of CNTs, as reported by Jin et al.[38] The other two catalysts, $S_{20}ZC_2$ and $S_{10}ZC_2$, showed 2150 and 1800 μmol h^{-1} g^{-1} hydrogen with the same CNT content, respectively.

3.5.2. Hydrogen Evolution over Time. Figure 8 displays the trend of photocatalytic hydrogen evolution with time under Ar plasma exposure. The reaction was initiated with a 10 kV AC supply at room temperature. The argon plasma exposure increased the reaction efficiency for H_2 production after different periods by splitting the H_2O molecules into H_2 and O_2 gas. The minimum gas production rate of 56 μmol h^{-1} g^{-1} was observed in the case of the PZO photocatalyst after 4 h of reaction. On the other hand, $S_{25}ZC_2$ exhibited the maximum
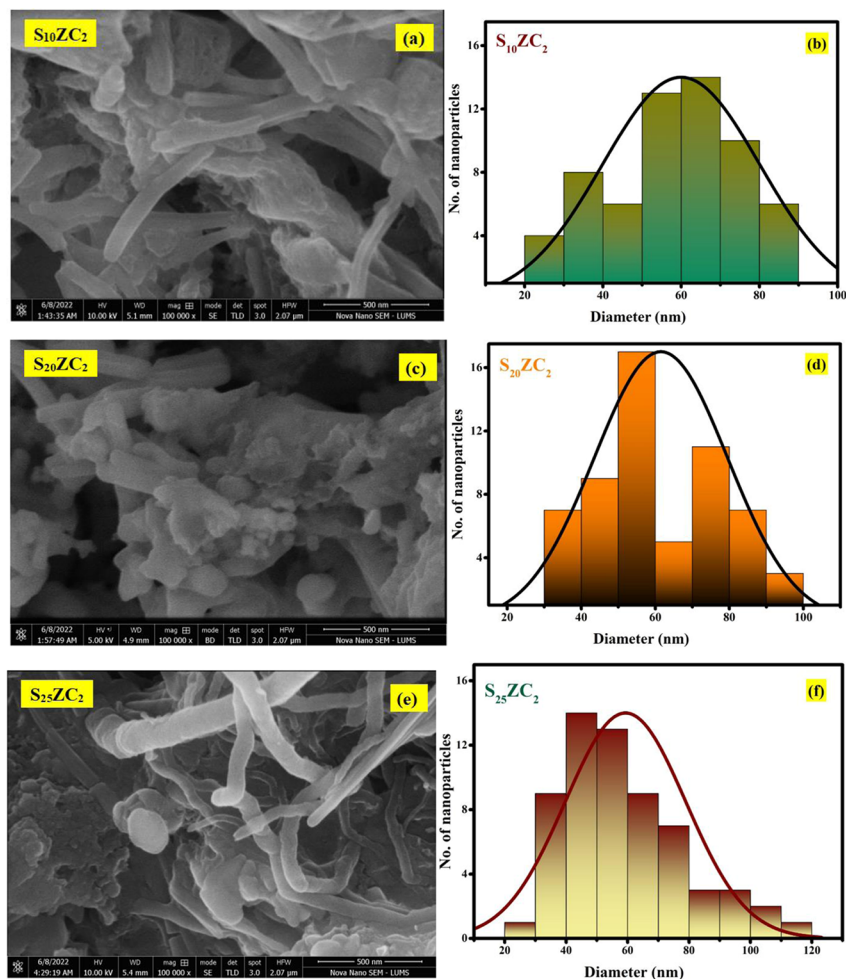
Figure 6. (a) SEM image of the sample $S_{10}ZC_2$, (b) diameter of $S_{10}ZC_2$, (c) SEM image of the sample $S_{20}ZC_2$, (d) diameter of $S_{20}ZC_2$, (e) SEM image of the sample $S_{25}ZC_2$, and (f) diameter of $S_{25}ZC_2$.
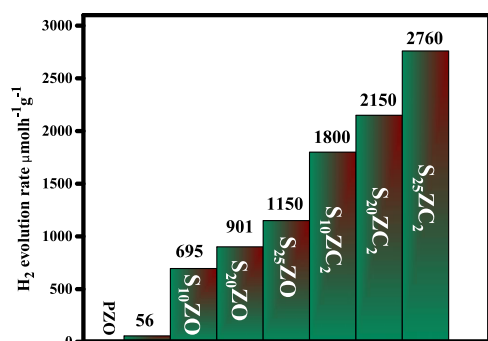

Figure 7. H_2 evolution rate of PZO, S_xZO ($S_{10}ZO$, $S_{20}ZO$, and $S_{25}ZO$), and $S_xZC_{x'}$ ($S_{10}ZC_2$, $S_{20}ZC_2$, and $S_{25}ZC_2$) photocatalysts.

Figure 8. H_2 evolution over PZO, S_xZO ($S_{10}ZO$, $S_{20}ZO$, and $S_{25}ZO$), and S_xZC_x ($S_{10}ZC_2$, $S_{20}ZC_2$, and $S_{25}ZC_2$) photocatalysts with time.

hydrogen evolution of 2760 μmol h^{-1} g^{-1} among all of the tested samples. The high hydrogen evolution efficiency of this photocatalyst was due to the introduction of CNTs and the maximum doping of Sr in PZO.[39,40] Figure 8 presents the direct relation of the released H_2 gas from nonthermal plasma over time.

3.5.3. Long-Term Reaction for Hydrogen Evolution. Figure 9 depicts the results of the H_2 evolution rate over the S_xZC_x photocatalyst as a function of time for long-term reaction runs. Four different readings were noted for each sample for this observation, showing the minimum evolution rates after 4 h.
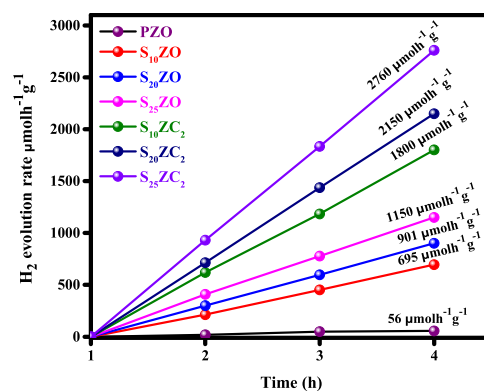
The hydrogen evolution with the $S_{25}ZC_2$ photocatalyst decreased from 2760 to 1670 μmol h^{-1} g^{-1}.[41] Similar experiments were carried out for the remaining catalysts ($S_{10}ZC_2$ and $S_{20}ZC_2$), which showed a hydrogen rate of 1800−1355 and 2150−1430 μmol h^{-1} g^{-1}, respectively. These outcomes showed an inverse relation between H_2 evolution and time that was opposite to the above relation in Figure 8. This is because the long-term reaction deactivated the
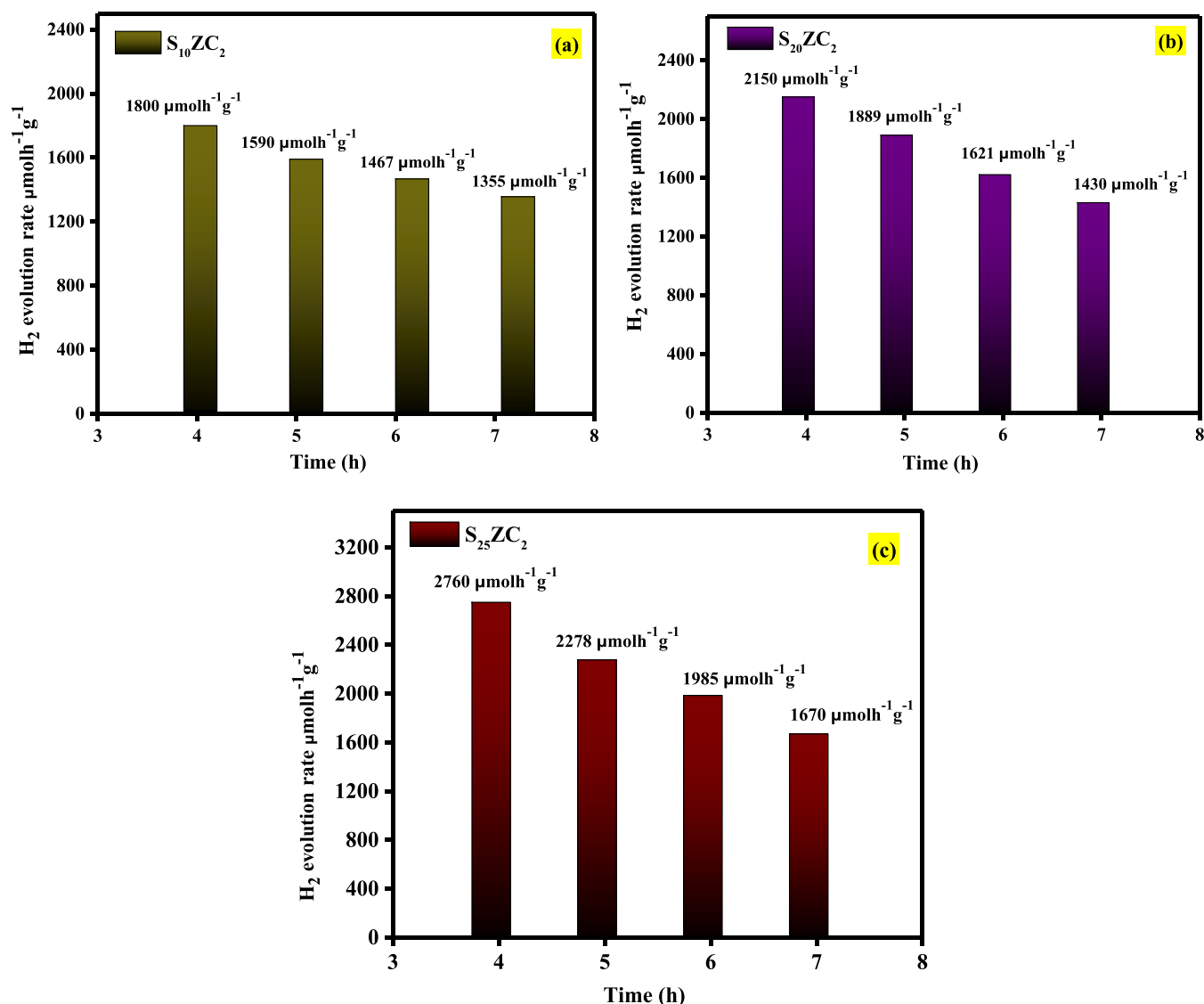
Figure 9. H_2 evolution with time over (a) $S_{10}ZC_2$, (b) $S_{20}ZC_2$, and (c) $S_{25}ZC_2$ photocatalysts.

photocatalyst, which decreased the hydrogen efficiency in nonthermal plasma revealed, as reported by Chen et al.[42]

3.6. Photocatalytic Mechanism. The photocatalytic mechanism of the Sr-doped ZnO/CNT photocatalyst for hydrogen production by water splitting under argon plasma is illustrated in Figure 10. Strontium (Sr) is an alkaline earth metal with a higher charge compensation ability and a different ionic radius than ZnO. Sr^{2+} has an ionic radius of 0.245 nm, which is much bigger than the ionic radius of Zn^{2+} (0.074 nm).[14] This discrepancy in ionic radii causes surface defects in the lattice of ZnO by producing variations in the photocatalyst's optical characteristics.[43−45] Sr doping can thus be used to alter the optical characteristics of ZnO. Yarahmadi et al.[45] used a Sr-doped ZnO photocatalyst to efficiently degrade synthetic dyes. The remarkable performance of the photocatalyst in degrading dyes was related to the development of defects in the ZnO lattice upon the introduction of Sr ions. Surface defects limit the rate of charge recombination and increase photocatalytic activity. A multilevel electron transfer system is created by combining tailored Sr, ZnO, and CNTs. Sr boosts light absorption in the ternary Sr-ZnO/CNT system by decreasing the band gap of ZnO. Because of their high
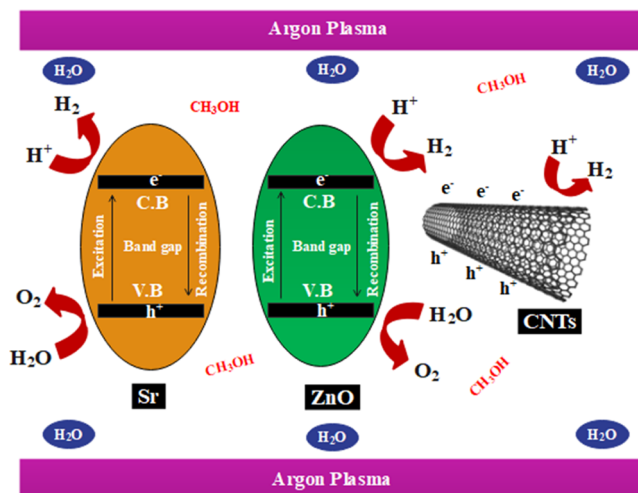

Figure 10. Photocatalytic mechanism of the Sr-doped ZnO/CNT photocatalyst for water splitting.

electrical conductivity, CNTs in the system reduce photo-corrosion and the rate of charge recombination.

When plasma radiation interacts with the catalyst, electrons are transferred to the conduction band of ZnO due to the photosensitizing effect. The electrons migrate to the conduction band of ZnO from the valence band by absorbing the energy equal to the band gap and leaving behind holes in the valence band. The reaction further proceeds between ZnO and Sr depending upon the difference of their work function. The published literature suggests that the work function of Sr is less than that of ZnO,[44,45] so the photoinduced electrons are trapped by Sr and cause maximum electron−hole pair separation. The water splits into H_2 and O_2 when the holes in the conduction band react with water molecules that form •OH radicals. When these •OH radicals react with methanol, they form the H^+ ions. As H^+ increases, the electrons of the conduction band are reduced to generate H_2 from methanol. The factors that control the photocatalytic H_2 evolution are the light assimilation toward the visible zone and charge separation. The capacity of CNTs to act as an electron acceptor and photosensitizer promotes faster electron conduction from the conduction band of ZnO to CNTs due to the latter's lower Fermi level, which helps to increase charge separation on the photocatalyst's surface.[46] Furthermore, the Sr-doped ZnO/CNT photocatalyst regulates the basicity of the photocatalyst surface and enhances the hydrogen production rate during water splitting.[47]

4. CONCLUSIONS

An atmospheric pressure DBD-based mercury-free light source was used to activate composite photocatalysts for water splitting into hydrogen fuel. The PZO, S_xZO ($S_{10}ZO$, $S_{20}ZO$, and $S_{25}ZO$), and S_xZC_x ($S_{10}ZC_2$, $S_{20}ZC_2$, and $S_{25}ZC_2$) photocatalysts were prepared by a facile sol−gel method. The structure morphology, band gap energy, functional groups, particle size, and electron−hole recombination rate were studied using XRD, UV−visible, FTIR, SEM, and PL analysis. The band gap energy of $S_{10}ZC_2$, $S_{20}ZC_2$, and $S_{25}ZC_2$ was measured to be about 2.27, 2.22, and 1.94 eV, respectively. The absorbance of photocatalysts showed a direct relation with the Sr doping content. PL analysis revealed low hole−electron recombination rate of the $S_{25}ZC_2$ photocatalyst among the tested photocatalysts. The minimum and maximum H_2 evolution rates were noted with PZO and $S_{25}ZC_2$ photocatalysts, respectively. The photocatalytic activity for H_2 production increased with concentrations such as PZO, $S_{10}ZO$, $S_{20}ZO$, $S_{25}ZO$, $S_{10}ZC_2$, $S_{20}ZC_2$, and $S_{25}ZC_2$ exhibited 56, 695, 901, 1150, 1800, 2150, and 2760 μmol h^{-1} g^{-1} hydrogen evolution, respectively. In the long-term reaction test, H_2 production first increased with time and then decreased. The decreasing rate occurred due to the deactivation of photocatalysts over time.

ASSOCIATED CONTENT

Data Availability Statement

The reported data is available from the corresponding authors on valid request.

AUTHOR INFORMATION

Corresponding Author

Muhammad Yasin Naz − *Department of Physics, University of Agriculture, Faisalabad 38040, Pakistan;* ● orcid.org/0000-0002-8490-7819; Email: yasin306@uaf.edu.pk

Authors

Muhammad Irfan − *Electrical Engineering Department, College of Engineering, Najran University, Najran 61441, Saudi Arabia;* ● orcid.org/0000-0003-4161-6875

Saba Afzal − *Department of Physics, University of Agriculture, Faisalabad 38040, Pakistan*

Muzammil Hussain − *Department of Physics, University of Agriculture, Faisalabad 38040, Pakistan*

Shazia Shukrullah − *Department of Physics, University of Agriculture, Faisalabad 38040, Pakistan;* ● orcid.org/0000-0002-4474-3768

Saifur Rahman − *Electrical Engineering Department, College of Engineering, Najran University, Najran 61441, Saudi Arabia*

Salim Nasar Faraj Mursal − *Electrical Engineering Department, College of Engineering, Najran University, Najran 61441, Saudi Arabia*

Abdulnour Ali Jazem Ghanim − *Civil Engineering Department, College of Engineering, Najran University, Najran 61441, Saudi Arabia*

Complete contact information is available at:
https://pubs.acs.org/10.1021/acsomega.3c01262

Notes

The authors declare no competing financial interest.

REFERENCES

(1) Ahmad, I.; Shukrullah, S.; Naz, M. Y.; Rasheed, M. A.; Ahmad, M.; Ahmed, E.; Akhtar, M. S.; Khalid, N. R.; Hussain, A.; Khalid, S. Boosted hydrogen evolution activity from Sr doped ZnO/CNTs nanocomposite as visible light driven photocatalyst. *Int. J. Hydrogen Energy* **2021**, *46*, 26711−26724.

(2) Dawood, F.; Shafiullah, G. M.; Anda, M. A hover view over Australia's Hydrogen Industry in recent history: the necessity for a Hydrogen Industry Knowledge-Sharing Platform. *Int. J. Hydrogen Energy* **2020**, *45*, 32916−32939.

(3) Bie, C.; Wang, L.; Yu, J. Challenges for photocatalytic overall water splitting. *Chem* **2022**, *8*, 1567−1574.

(4) Galdámez-Martínez, A.; Bai, Y.; Santana, G.; Sprick, R. S.; Dutt, A. Photocatalytic hydrogen production performance of 1-D ZnO nanostructures: role of structural properties. *Int. J. Hydrogen Energy* **2020**, *45*, 31942−31951.

(5) Bahadoran, A.; Masudy-Panah, S.; De Lile, J. R.; Li, J.; Gu, J.; Sadeghi, B.; Ramakrishna, S.; Liu, Q. Novel 0D/1D $ZnBi_2O_4$/ZnO S-scheme photocatalyst for hydrogen production and BPA removal. *Int. J. Hydrogen Energy* **2021**, *46*, 24094−24106.

(6) Ramírez-Ortega, D.; Guerrero-Araque, D.; Acevedo-Peña, P.; Reguera, E.; Calderon, H. A.; Zanella, R. Enhancing the photocatalytic hydrogen production of the ZnO−TiO_2 heterojunction by supporting nanoscale Au islands. *Int. J. Hydrogen Energy* **2021**, *46*, 34333−34343.

(7) Esmaeilzadeh, O.; Eivani, A. R.; Mehdizade, M.; Boutorabi, S. M. A.; Masoudpanah, S. M. An investigation of microstructural

background for improved corrosion resistance of WE43 magnesium-based composites with ZnO and Cu/ZnO additions. *J. Alloys Compd.* **2022**, *908*, No. 164437.

(8) Yarahmadi, M.; Maleki-Ghaleh, H.; Mehr, M. E.; Dargahi, Z.; Rasouli, F.; Siadati, M. H. Synthesis and characterization of Sr-doped ZnO nanoparticles for photocatalytic applications. *J. Alloys Compd.* **2021**, *853*, No. 157000.

(9) Samadzadeh, A.; Sheikhshoaie, I.; Karimi-Maleh, H. Simultaneous determination of epinephrine and tyrosine using a glassy carbon electrode amplified with ZnO-Pt/CNTs nanocomposite. *Curr. Anal. Chem.* **2019**, *15*, 166−171.

(10) Zhang, Y. S.; Zhu, H. L.; Yao, D.; Williams, P. T.; Wu, C.; Xu, D.; Hu, Q.; Manos, G.; Yu, L.; Zhao, M.; Shearing, P. R.; Brett, D. J. L. Thermo-chemical conversion of carbonaceous wastes for CNT and hydrogen production: a review. *Sustainable Energy Fuels* **2021**, *5*, 4173−4208.

(11) Huang, C.; Ouyang, T.; Zou, Y.; Li, N.; Liu, Z. Q. Ultrathin NiCo₂Pₓ nanosheets strongly coupled with CNTs as efficient and robust electrocatalysts for overall water splitting. *J. Mater. Chem. A* **2018**, *6*, 7420−7427.

(12) Otaegi, I.; Aranburu, N.; Iturrondobeitia, M.; Ibarretxe, J.; Guerrica-Echevarría, G. The effect of the preparation method and the dispersion and aspect ratio of CNTs on the mechanical and electrical properties of bio-based polyamide-4, 10/CNT nanocomposites. *Polymers* **2019**, *11*, No. 2059.

(13) Hümmer, T.; Noe, J.; Hofmann, M. S.; Hänsch, T. W.; Högele, A.; Hunger, D. Cavity-enhanced Raman microscopy of individual carbon nanotubes. *Nat. Commun.* **2016**, *7*, No. 12155.

(14) Ahmad, I.; Shukrullah, S.; Naz, M. Y.; Ahmed, E.; Ahmad, M. Rare earth metals co-doped ZnO/CNTs composite as high performance photocatalyst for hydrogen production from water_-triethanolmine mixture. *Int. J. Hydrogen Energy* **2022**, *47*, 9283−9294.

(15) Lin, W. C.; Yang, W. D.; Huang, I. L.; Wu, T. S.; Chung, Z. J. Hydrogen Production from Methanol/Water Photocatalytic Decomposition Using Pt/TiO₂₋ₓNₓ Catalyst. *Energy Fuels* **2009**, *23*, 2192−2196.

(16) Xiang, Q.; Ma, X.; Zhang, D.; Zhou, H.; Liao, Y.; Zhang, H.; Xu, S.; Levchenko, I.; Bazaka, K. Interfacial modification of titanium dioxide to enhance photocatalytic efficiency towards H₂ production. *J. Colloid Interface Sci.* **2019**, *556*, 376−385.

(17) Kawawaki, T.; Kataoka, Y.; Ozaki, S.; Kawachi, M.; Hirata, M.; Negishi, Y. Creation of active water-splitting photocatalysts by controlling cocatalysts using atomically precise metal nanoclusters. *Chem. Commun.* **2021**, *57*, 417−440.

(18) Yao, X.; Zhang, Y.; Wei, Z.; Chen, M.; Shangguan, W. Plasma-Catalytic Conversion of CO₂ and H₂O into H₂, CO, and Traces of CH₄ over NiO/Cordierite Catalysts. *Ind. Eng. Chem. Res.* **2020**, *59*, 19133−19144.

(19) El-Shafie, M.; Kambara, S.; Hayakawa, Y. Comprehensive assessment of hydrogen production in argon-water vapors plasmolysis. *Energy Sci. Eng.* **2021**, *9*, 267−283.

(20) Hench, L. L.; West, J. K. The sol-gel process. *Chem. Rev.* **1990**, *90*, 33−72.

(21) Hao, L.; Kamboh, M. A.; Su, Y.; Wang, L.; Zhang, M.; Zhang, J.; Wang, Q. Ab initio study of the electronic, optical, and water-splitting properties of Fe-doped ZnO monolayer. *Phys. E* **2022**, *137*, No. 115059.

(22) Li, W.; Meng, S.; Li, Z.; Song, H. The function of porous working electrodes for hydrogen production from water splitting in non-thermal plasma reactor. *Fuel* **2022**, *310*, No. 122156.

(23) Prakash, R.; Hossain, A. M.; Pal, U. N.; Kumar, N.; Khairnar, K.; Mohan, M. K. Dielectric Barrier Discharge based Mercury-free plasma UV-lamp for efficient water disinfection. *Sci. Rep.* **2017**, *7*, No. 17426.

(24) Kumaran, N. N.; Muraleedharan, K. Photocatalytic activity of ZnO and Sr²⁺ doped ZnO nanoparticles. *J. Water Process Eng.* **2017**, *17*, 264−270.

(25) Beena, V.; Rayar, S. L.; Ajitha, S.; Ahmad, A.; Albaqami, M. D.; Alsabar, F. A. A.; Sillanpää, M. Synthesis and characterization of Sr-

doped ZnSe nanoparticles for catalytic and biological activities. *Water* **2021**, *13*, No. 2189.

(26) Neena, D.; Humayun, M.; Bhattacharyya, D.; Fu, D. Hierarchical Sr-ZnO/g-C₃N₄ heterojunction with enhanced photocatalytic activities. *J. Photochem. Photobiol., A* **2020**, *396*, No. 112515.

(27) Park, B. H.; Park, H.; Kim, T.; Yoon, S. J.; Kim, Y.; Son, N.; Kang, M. S-scheme assisted Cu₂O/ZnO flower-shaped heterojunction catalyst for breakthrough hydrogen evolution by water splitting. *Int. J. Hydrogen Energy* **2021**, *46*, 38319−38335.

(28) Suwanboon, S.; Somraksa, W.; Amornpitoksuk, P.; Randorn, C. Effect of trisodium citrate on the formation and structural, optical and photocatalytic properties of Sr-doped ZnO. *J. Alloys Compd.* **2020**, *832*, No. 154963.

(29) Kaskun, S.; Akinay, Y.; Kayfeci, M. Improved hydrogen adsorption of ZnO doped multi-walled carbon nanotubes. *Int. J. Hydrogen Energy* **2020**, *45*, 34949−34955.

(30) Savari, R.; Rouhi, J.; Fakhar, O.; Kakooei, S.; Pourzadeh, D.; Jahanbakhsh, O.; Shojaei, S. Development of photo-anodes based on strontium doped zinc oxide-reduced graphene oxide nanocomposites for improving performance of dye-sensitized solar cells. *Ceram. Int.* **2021**, *47*, 31927−31939.

(31) Akram, R.; Almohaimeed, Z. M.; Bashir, A.; Ikram, M.; Qadir, K. W.; Zafar, Q. Synthesis and characterization of pristine and strontium-doped zinc oxide nanoparticles for methyl green photodegradation application. *Nanotechnology* **2022**, *33*, No. 295702.

(32) Raghavendra, P. V.; Bhat, J. S.; Deshpande, N. G. Enhancement of photoluminescence in Sr doped ZnO thin films prepared by spray pyrolysis. *Mater. Sci. Semicond. Process.* **2017**, *68*, 262−269.

(33) Pradeev Raj, K.; Sadaiyandi, K.; Kennedy, A.; Thamizselvi, R. Structural, optical, photoluminescence and photocatalytic assessment of Sr-doped ZnO nanoparticles. *Mater. Chem. Phys.* **2016**, *183*, 24−36.

(34) Cursaru, L. M.; Valsan, S. N.; Puscasu, M. E.; Tudor, I. A.; Zarnescu-Ivan, N.; Vasile, B. S.; Piticescu, R. M. Study of ZnO-CNT Nanocomposites in High-Pressure Conditions. *Materials* **2021**, *14*, No. 5330.

(35) Saad, R.; Gamal, A.; Zayed, M.; Ahmed, A. M.; Shaban, M.; BinSabt, M.; Rabia, M.; Hamdy, H. Fabrication of ZnO/CNTs for application in CO₂ sensor at room temperature. *Nanomaterials* **2021**, *11*, No. 3087.

(36) Peña-Garcia, R.; Guerra, Y.; Castro-Lopes, S.; Camejo, Y. M.; Soares, J. M.; Franco, A., Jr.; Padrón-Hernández, E.; Cabrera-Baez, M. Morphological, magnetic and EPR studies of ZnO nanostructures doped and co-doped with Ni and Sr. *Ceram. Int.* **2021**, *47*, 28714−28722.

(37) Yoo, H.; Kahng, S.; Kim, J. H. Z-scheme assisted ZnO/Cu₂O-CuO photocatalysts to increase photoactive electrons in hydrogen evolution by water splitting. *Sol. Energy Mater. Sol. Cells* **2020**, *204*, No. 110211.

(38) Jin, J.; Fu, M.; Wang, L.; Ma, T.; Li, X.; Jin, F.; Lu, Y. Water-splitting mechanism analysis of Sr/Ca doped LaFeO₃ towards commercial efficiency of solar thermochemical H₂ production. *Int. J. Hydrogen Energy* **2021**, *46*, 1634−1641.

(39) Luo, Y.; Yang, Y.; Lin, Y.; Tian, Y.; Wu, L.; Yang, L.; Hou, X.; Zheng, C. Low-temperature and atmospheric pressure sample digestion using dielectric barrier discharge. *Anal. Chem.* **2018**, *90*, 1547−1553.

(40) Phoon, B. L.; Lai, C. W.; Juan, J. C.; Show, P. L.; Pan, G. T. Recent developments of strontium titanate for photocatalytic water splitting application. *Int. J. Hydrogen Energy* **2019**, *44*, 14316−14340.

(41) Jain, S. K.; Pandit, N. A.; Fazil, M.; Ali, S. A.; Ahmed, J.; Alshehri, S. M.; Mao, Y.; Ahmad, T. Chemical Fabrication, Structural Characterization and Photocatalytic Water Splitting Application of Sr-Doped SnO₂ Nanoparticles. *Nanotechnology* **2022**, *33*, No. 355706.

(42) Chen, G.; Hu, Z.; Zhu, Y.; Gu, B.; Zhong, Y.; Lin, H. J.; Chen, C. T.; Zhou, W.; Shao, Z. A universal strategy to design superior water-splitting electrocatalysts based on fast in situ reconstruction of amorphous nanofilm precursors. *Adv. Mater.* **2018**, *30*, No. 1804333.

(43) Toranjizadeh, H.; Shabani, P.; Ramezani, A. Enhancement of ethanol gas sensing mechanism at high humidity levels and optical

features using Sr-doped ZnO NPs. *J. Mater. Sci.: Mater. Electron.* **2019**, *30*, 14167−14181.

(44) Shkir, M.; Al-Shehri, B. M.; Pachamuthu, M. P.; Khan, A.; Chandekar, K. V.; AlFaify, S.; Hamdy, M. S. A remarkable improvement in photocatalytic activity of ZnO nanoparticles through Sr doping synthesized by one pot flash combustion technique for water treatments. *Colloids Surf., A* **2020**, *587*, No. 124340.

(45) Yarahmadi, M.; Maleki-Ghaleh, H.; Mehr, M. E.; Dargahi, Z.; Rasouli, F.; Siadati, M. H. Synthesis and characterization of Sr-doped ZnO nanoparticles for photocatalytic applications. *J. Alloys Compd.* **2021**, *853*, No. 157000.

(46) Sharma, A.; Watkins, S. E.; Andersson, G.; Lewis, D. A. Effect of annealing temperature of ZnO on the energy level alignment in inverted organic photovoltaics (OPVs). *Energy Technol.* **2014**, *2*, 462−468.

(47) Ghasemipour, P.; Fattahi, M.; Rasekh, B.; Yazdian, F. Developing the ternary ZnO doped MoS$_2$ nanostructures grafted on CNT and reduced graphene oxide (RGO) for photocatalytic degradation of aniline. *Sci. Rep.* **2020**, *10*, No. 4414.

■ NOTE ADDED AFTER ASAP PUBLICATION

This paper originally published ASAP on May 10, 2023. A correction was made in first paragraph of section 2.2 and a new version reposted on May 15, 2023.